AIMS Mathematics

https://www.aimspress.com/journal/Math

AIMS Mathematics, 11(8): 27304–27326.
DOI: 10.3934/math.20261902
Received: 01 July 2026
Revised: 07 August 2026
Accepted: 11 August 2026
Published: 28 August 2026

Research article

Phase-plane dynamics and nonlinear traveling-wave patterns in a (3+1)-dimensional mKdV-ZK equation

Jiaye Lin[1], **Yaling Lai**[1], **Xiyan Wu**[1], **Changlong Chen**[2], **Yucheng Chen**[1,*] **and Junjie Li**[1,*]

[1] School of Mathematics and Statistics, Xiamen University of Technology, Xiamen 361024, China

[2] College of Computer and Information Engineering, Xiamen University of Technology, Xiamen 361024, China

* **Correspondence:** Email: ycchen@xmut.edu.cn, lijunjie@xmut.edu.cn.

Abstract: Traveling waves of the (3+1)-dimensional modified Korteweg-de Vries-Zakharov-Kuznetsov equation are studied, first in the unforced case and then under a weak co-moving periodic source. Without forcing, the profile equation reduces to a quartic Hamiltonian whose level sets carry periodic waves, homoclinic pulses, heteroclinic kinks, and unbounded orbits. The substitution $\Phi = U^2$ turns the first integral into a cubic polynomial and gives a discriminant-based classification of a restricted family of explicit profiles subject to the constraint $\Phi \geq 0$ and to a piecewise sign reconstruction of U. This part recovers structures already reported in bifurcation studies of the same model and serves as the geometric baseline. The forced problem is the main concern. A weak periodic source turns the reduction into a Duffing-type system for which closed-form Melnikov functions are obtained on both the homoclinic and the heteroclinic separatrix. Both have simple zeros, so both separatrices split transversely at a small forcing amplitude. Their amplitudes differ where it matters: The heteroclinic one tends to a finite positive limit as $\omega \to 0$, the homoclinic one vanishes there and peaks at an intermediate frequency, and both decay exponentially at high frequency. Stroboscopic Poincaré sections and largest Lyapunov exponents computed at $\varepsilon = 0.01, 0.05,$ and 0.10 agree with this picture, the section passing from thin invariant arcs to a scattered layer around the former figure-eight as the exponent rises from order 10^{-4} to about 0.12.

Keywords: traveling-wave solution; bifurcation analysis; Melnikov analysis; chaotic dynamics; Hamiltonian system
Mathematics Subject Classification: 35Q53, 35C07

1. Introduction

The modified Zakharov-Kuznetsov (ZK) equation extends the dispersive balance of Korteweg-de Vries (KdV)-type models to multidimensional media in which transverse effects cannot be neglected [1–3]. Related traveling-wave and lump structures in higher-dimensional dispersive models have also been reported [4]. Its cubic nonlinearity is relevant when the quadratic response is weak or changes sign, as occurs in several magnetized-plasma and nonlinear-wave settings. For a traveling wave, the PDE reduces to an autonomous ordinary differential equation, and the resulting phase portrait records the admissible bounded oscillations and separatrix connections [5–7]. Closed trajectories generate periodic waves, homoclinic loops generate localized pulses, and heteroclinic connections produce kink-type profiles.

Extending from one to higher dimensions, the Kadomtsev-Petviashvili (KP) equation [8] and the Zakharov-Kuznetsov equation [9] were successively developed as generalizations of the one-dimensional Korteweg-de Vries equation. The KdV equation itself [10] is a cornerstone model for weakly nonlinear long waves in one dimension; its higher-dimensional generalizations become necessary when transverse effects are significant [11]. Among these, the ZK equation extends the KdV balance to multidimensional settings and is frequently employed in magnetized plasma contexts [12]. However, in certain physical regimes, the dominant nonlinearity may shift from quadratic to cubic, rendering the classical ZK equation insufficient to fully capture wave evolution [13]. In such cases, a cubic nonlinear term must be incorporated [11, 14, 15]. Moreover, the intrinsically three-dimensional nature of real physical space demands a model that includes all three spatial coordinates, making the (3+1)-dimensional form a natural framework for describing such wave propagation [16–18]. Motivated by these considerations, this article investigates the (3+1)-dimensional modified ZK model with a cubic nonlinearity, namely the mKdV-ZK equation:

$$u_t + \mu_1 u^2 u_x + \mu_2 u_{xxx} + \mu_3 (u_{yy} + u_{zz})_x = 0, \tag{1.1}$$

where the parameters μ_1, μ_2, and μ_3 characterize the cubic nonlinearity strength, the longitudinal dispersion coefficient, and the transverse coupling effect, respectively.

For the unforced mKdV-ZK equation, traveling-wave solutions and bifurcation structures have been obtained by direct ansatz and auxiliary-equation methods [19–21], by expansion and Kudryashov-type schemes [22–24], and by elliptic-function and planar-dynamical-system analyses [25–27]; related soliton and bifurcation studies of ZK-type models are reported in [28, 29]. In particular, [30] analysed the bifurcations of traveling-wave solutions of the (3+1)-dimensional mKdV-ZK equation, while [31] studied bifurcations and exact solutions of the generalized KdV-ZK equation, and [32] investigated solitary waves and chaotic behaviors in related systems. These studies established much of the current understanding of unforced wave geometry. Less attention has been paid to the fate of the homoclinic and heteroclinic boundaries when the reduced dynamics is subjected to a weak periodic modulation. This distinction is important: The unforced phase portrait identifies the coherent wave families, whereas a separatrix-splitting calculation determines whether those organizing boundaries persist under external excitation.

The unforced reduction is used here as a geometric baseline, not as the novel part. What is new concerns the forced system. A periodic source compatible with the co-moving reduction is added, and the Melnikov function is evaluated separately on the homoclinic the heteroclinic separatrices, in the spirit of earlier applications to nonlinear wave equations [33, 34]. The computation follows the classical Melnikov framework [35–37], as presented in [38]. This yields two explicit transverse-splitting criteria and shows that the two separatrices respond differently to the forcing frequency. Phase portraits, stroboscopic Poincaré sections and largest Lyapunov exponents are then used to test this prediction at three representative weak-forcing amplitudes, and the numerical results are found to be consistent with the Melnikov mechanism.

Recent work has continued along related directions, including exact-wave construction by sub-equation and Exp-function techniques [39–41], phase-space and perturbation analysis [42], and fractional or stochastic extensions that are closer to the present nonlinear-wave setting [16, 34]. These studies provide useful context, whereas the question addressed here is specifically the separatrix splitting of the periodically forced mKdV-ZK reduction.

The remainder of the article is organized as follows. Section 2 derives the traveling wave reduction and first integral. Section 3 constructs explicit traveling wave solutions using discriminant-based classification. Section 4 presents a complete four-quadrant Hamiltonian phase portrait classification, including equilibrium analysis, four canonical configurations, and explicit homoclinic/heteroclinic formulas for the separatrix thresholds. Section 5 presents a Melnikov analysis to analytically justify the onset of chaos under periodic forcing via transverse separatrix splitting. Section 6 numerically investigates chaotic dynamics and sensitivity to initial conditions. Section 7 concludes the article.

2. Traveling wave transformation and first integral

This section derives the autonomous traveling-wave equation and the first integral used in the subsequent phase-plane analysis. The integration constant is retained initially so that the restriction adopted later can be stated explicitly.

2.1. Traveling wave transformation

Consider the modified KdV-ZK equation:

$$u_t + \mu_1 u^2 u_x + \mu_2 u_{xxx} + \mu_3 (u_{yy} + u_{zz})_x = 0, \tag{2.1}$$

where the parameters μ_1, μ_2, and μ_3 are as defined in the introduction. Applying the traveling wave transformation $u(x, y, z, t) = U(\xi)$ with $\xi = kx + ly + mz - ct$ and substituting the derivatives into Eq (2.1) yields

$$-cU' + \mu_1 k U^2 U' + \mu_2 k^3 U''' + \mu_3 k(l^2 + m^2)U''' = 0. \tag{2.2}$$

Define

$$A = \mu_2 k^3 + \mu_3 k(l^2 + m^2) = k[\mu_2 k^2 + \mu_3 (l^2 + m^2)].$$

Integrating Eq (2.2) once with respect to ξ gives

$$AU'' - cU + \frac{\mu_1 k}{3} U^3 = C_0, \tag{2.3}$$

where C_0 is the integration constant. The analysis below is restricted to $C_0 = 0$. This choice preserves the symmetry $U \mapsto -U$, keeps $U = 0$ as an equilibrium, and contains the zero-background homoclinic and heteroclinic branches considered in Sections 4 and 5. When $C_0 \neq 0$, a linear term tilts the effective potential, the equilibria move off the symmetric configuration, and the four-quadrant classification no longer applies.

Letting $Y = U'$, the equivalent planar dynamical system is obtained:

$$\begin{cases} \dfrac{dU}{d\xi} = Y, \\ \dfrac{dY}{d\xi} = \dfrac{c}{A}\,U - \dfrac{\mu_1 k}{3A}\,U^3. \end{cases} \tag{2.4}$$

2.2. Hamiltonian

Multiplying the second-order equation by U' and integrating yields the first integral:

$$H(U,Y) = \frac{1}{2}Y^2 - \frac{c}{2A}U^2 + \frac{\mu_1 k}{12A}U^4 = E, \tag{2.5}$$

where E denotes the conserved energy level of the traveling-wave ordinary differential equation (ODE). Here, H is an energy-like invariant in the co-moving coordinate, not necessarily the total laboratory-frame energy of the plasma. Its kinetic part $Y^2/2$ and its effective potential fix the equilibria, the bounded oscillations, and the separatrix connections, so the level sets of H can be read directly as a catalog of wave profiles. Hamiltonian-based frequency formulations have also been used to obtain approximate frequency–amplitude relations for strongly nonlinear oscillators [43,44]. The construction used here is different: H in Eq (2.5) is an exact first integral of the reduced profile equation, not an approximate energy functional built for frequency estimation.

3. Traveling wave solutions

3.1. Reduction transformation

To simplify the analysis, the transformation $\Phi = U^2$ is introduced, which converts the quartic term in the Hamiltonian Eq (2.5) into a cubic form. Let

$$\Phi(\xi) = U^2(\xi) \quad (\Phi \geq 0). \tag{3.1}$$

The first integral contains only even powers of U. Introducing $\Phi = U^2$ therefore converts the quartic energy polynomial into a cubic polynomial, which is convenient for a complete discriminant classification. The forward map loses nothing, but its inverse does: $U = \pm\sqrt{\Phi}$ is two-to-one and requires $\Phi \geq 0$, so a fixed sign recovers only constant-sign branches, and a profile crossing $U = 0$ has to be rebuilt piecewise across its zeros. Every formal solution of the cubic must therefore be tested against $\Phi(\xi) \geq 0$.

Then, $\Phi' = 2UU'$. On any interval on which $U \neq 0$ (equivalently $\Phi > 0$), the relation can be inverted to give

$$U' = \frac{1}{2\sqrt{\Phi}}\Phi'. \tag{3.2}$$

At a zero of U, the inverse sign must be reconstructed piecewise, and the relation is interpreted by continuity.

Substituting Eqs (3.1) and (3.2) into the Hamiltonian Eq (2.5) yields

$$\frac{1}{4\Phi}(\Phi')^2 = -\frac{\mu_1 k}{6A}\Phi^2 + \frac{c}{A}\Phi + 2E, \tag{3.3}$$

and rearranging gives

$$(\Phi')^2 = -\frac{2\mu_1 k}{3A}\Phi^3 + \frac{4c}{A}\Phi^2 + 8E\Phi. \tag{3.4}$$

For convenience, our work introduces the following notations:

$$\alpha = -\frac{2\mu_1 k}{3A}, \quad \beta = \frac{4c}{A}, \quad \gamma = 8E \tag{3.5}$$

so that Eq (3.4) becomes

$$(\Phi')^2 = \alpha\Phi^3 + \beta\Phi^2 + \gamma\Phi, \tag{3.6}$$

where $\alpha \neq 0$ is required; otherwise, the equation degenerates to a quadratic form.

3.2. Standard form conversion

To eliminate the quadratic term and obtain a standard cubic form, a linear shift transformation is applied: $\Phi = \lambda\Psi + \eta$. Substituting this into Eq (3.6) gives

$$\lambda^2(\Psi')^2 = \alpha(\lambda\Psi + \eta)^3 + \beta(\lambda\Psi + \eta)^2 + \gamma(\lambda\Psi + \eta), \tag{3.7}$$

and expanding yields

$$\lambda^2(\Psi')^2 = \alpha\lambda^3\Psi^3 + (3\alpha\lambda^2\eta + \beta\lambda^2)\Psi^2 + (3\alpha\lambda\eta^2 + 2\beta\lambda\eta + \gamma\lambda)\Psi + (\alpha\eta^3 + \beta\eta^2 + \gamma\eta). \tag{3.8}$$

Dividing by λ^2 and comparing with the target form $(\Psi')^2 = \Psi^3 + \chi_1\Psi + \chi_0$, the coefficient of Ψ^3 is set to 1, and the coefficient of Ψ^2 is set to 0:

$$\begin{cases} \alpha\lambda = 1, \\ 3\alpha\eta + \beta = 0. \end{cases} \tag{3.9}$$

Solving these conditions gives

$$\lambda = \frac{1}{\alpha}, \quad \eta = -\frac{\beta}{3\alpha}. \tag{3.10}$$

With these choices, the remaining coefficients become χ_1 and χ_0. Substituting λ, η and simplifying yields

$$\chi_1 = -\frac{16}{3A^2}(c^2 + A\mu_1 kE), \tag{3.11}$$

$$\chi_0 = \frac{128}{27A^3}\left(c^3 + \frac{3A\mu_1 kcE}{2}\right). \tag{3.12}$$

Thus, Eq (3.6) is transformed into the standard form:

$$(\Psi')^2 = \Psi^3 + \chi_1\Psi + \chi_0. \tag{3.13}$$

3.3. Classification of solutions via discriminant

Explicit profiles of Eq (2.1) have also been constructed by subequation and Exp-function techniques [39, 40]. Those approaches generate individual closed-form solutions efficiently. The route used here is complementary: The complete discriminant system organizes the profiles by the root pattern of the cubic, so that each formula can afterwards be matched to a closed orbit, a separatrix, or an unbounded branch of the Hamiltonian in Section 4.

Equation (3.13) involves the square root of a cubic polynomial. Integrals of this type are evaluated using elliptic integrals. For the cubic $\Psi^3 + \chi_1\Psi + \chi_0 = 0$, the complete discriminant system provides a systematic classification of the roots. The discriminant is $\Delta = -4\chi_1^3 - 27\chi_0^2$. Depending on the sign of Δ, the cubic has three distinct real roots, multiple roots, or one real root and two complex conjugate roots. Each case leads to a different functional form for $\Psi(\xi)$ and consequently for $U(\xi)$. Recall that

$$\Phi = \alpha^{-1}\Psi - \frac{\beta}{3\alpha}, \qquad U = \pm\sqrt{\Phi}, \tag{3.14}$$

and all branches are subject to the admissibility condition stated in Section 3.1. Each case is treated separately.

Case I ($\Delta > 0, \chi_1 < 0$): Three distinct real roots $e_1 > e_2 > e_3$.

When $\Delta > 0$, the inequality $-4\chi_1^3 > 27\chi_0^2$ holds, which requires $\chi_1 < 0$. From $\chi_1 < 0$, the parameter condition $c^2 + A\mu_1 kE > 0$ follows. Write

$$P(\Psi) = (\Psi - e_1)(\Psi - e_2)(\Psi - e_3), \qquad e_1 > e_2 > e_3. \tag{3.15}$$

Then,

$$\Psi(\xi) = e_3 + (e_2 - e_3)\,\mathrm{sn}^2\left[\frac{1}{2}\sqrt{e_1 - e_3}(\xi - \xi_0); m_e\right], \qquad m_e = \frac{e_2 - e_3}{e_1 - e_3}. \tag{3.16}$$

Here m_e denotes the elliptic parameter (the square of the modulus), which is the convention used consistently throughout this section. This branch is bounded in $[e_3, e_2]$ and corresponds to a periodic wave. An equivalent representation using cn^2 is possible but requires a phase shift to keep the root interval consistent.

Case II ($\Delta = 0$): Multiple-root branches.

The condition $\Delta = 0$ implies $\chi_0^2 = -4\chi_1^3/27$ with $\chi_1 \le 0$.

(a) Triple root ($\chi_1 = \chi_0 = 0$):

From $\chi_1 = \chi_0 = 0$, it follows that

$$c^2 + A\mu_1 kE = 0, \quad \text{and} \quad c^3 + \frac{3A\mu_1 kcE}{2} = 0,$$

which imply $c = 0$ and $E = 0$. Hence, $P(\Psi) = \Psi^3$. The nonconstant solution is

$$\Psi(\xi) = \frac{4}{(\xi - \xi_0)^2}, \tag{3.17}$$

together with the constant solution $\Psi \equiv 0$.

(b) Double root above the simple root ($e_1 = e_2 = a > e_3 = b$):

$$P(\Psi) = (\Psi - a)^2(\Psi - b). \tag{3.18}$$

The bounded homoclinic branch is

$$\Psi(\xi) = a - (a-b)\,\mathrm{sech}^2\left[\frac{1}{2}\sqrt{a-b}\,(\xi-\xi_0)\right]. \tag{3.19}$$

There is also an unbounded singular branch,

$$\Psi(\xi) = a + (a-b)\,\mathrm{csch}^2\left[\frac{1}{2}\sqrt{a-b}\,(\xi-\xi_0)\right]. \tag{3.20}$$

(c) Double root below the simple root ($e_1 = a > e_2 = e_3 = b$)**:**

$$P(\Psi) = (\Psi - a)(\Psi - b)^2. \tag{3.21}$$

The solution is a singular periodic branch:

$$\Psi(\xi) = a + (a-b)\tan^2\left[\frac{1}{2}\sqrt{a-b}\,(\xi-\xi_0)\right]. \tag{3.22}$$

Case III ($\Delta < 0$)**: One real root** r **and two complex conjugates** $p \pm iq$**.**

From the cubic equation, Vieta's relations give

$$r + 2p = 0 \quad \Rightarrow \quad p = -\frac{r}{2}, \qquad q^2 = -\left(\frac{3r^2}{4} + \chi_1\right). \tag{3.23}$$

The cubic factorizes as

$$P(\Psi) = (\Psi - r)[(\Psi - p)^2 + q^2]. \tag{3.24}$$

Introduce the auxiliary quantities

$$S = \sqrt{(r-p)^2 + q^2}, \qquad m_e = \frac{1}{2}\left[1 - \frac{r-p}{S}\right]. \tag{3.25}$$

With these definitions, the solution for $\Psi(\xi)$ takes the form of a singular elliptic branch,

$$\Psi(\xi) = r - S + \frac{2S}{1 + \mathrm{cn}\left[\sqrt{S}\,(\xi-\xi_0); m_e\right]}. \tag{3.26}$$

This branch is singular when the denominator $1 + \mathrm{cn}(\cdot; m_e)$ vanishes, which occurs at discrete points

$$\xi = \xi_0 + \frac{2}{\sqrt{S}}(2n+1)K(m_e), \quad n \in \mathbb{Z},$$

where $K(m_e)$ is the complete elliptic integral of the first kind. On intervals excluding these singularities, the solution is real-valued and represents a periodic wave with unbounded amplitude near the poles. The corresponding $U(\xi) = \pm\sqrt{\Phi(\xi)}$ is admissible only where $\Phi(\xi) = \alpha^{-1}\Psi(\xi) - \beta/(3\alpha) \geq 0$, subject to the condition stated in Section 3.1.

3.4. Numerical simulation and residual verification

The simulations below use dimensionless parameters $\mu_1 = 1.0$, $\mu_2 = 1.0$, $\mu_3 = 0.5$, $k = 1.0$, $l = 0.5$, and $m = 0.3$, giving

$$A = k[\mu_2 k^2 + \mu_3(l^2 + m^2)] = 1.17.$$

These parameters are chosen as mathematical illustrations and are not calibrated against a specific plasma experiment. Each retained profile is then checked twice: symbolically, by substituting $U(\xi)$ into the reduced ODE Eq (2.3) with a computer-algebra system and simplifying the residual under the corresponding root conditions and then numerically, by evaluating the residual on a fine grid away from the singular points.

For the periodic wave in Figure 1 for $\Delta > 0$, the residual satisfies $\max |R| \approx 2.3 \times 10^{-12}$. For the solitary wave in Figure 2 for $\Delta = 0$, the residual satisfies $\max |R| \approx 1.7 \times 10^{-12}$. Both values sit at the round-off level of double-precision arithmetic. These results illustrate two representative regimes.

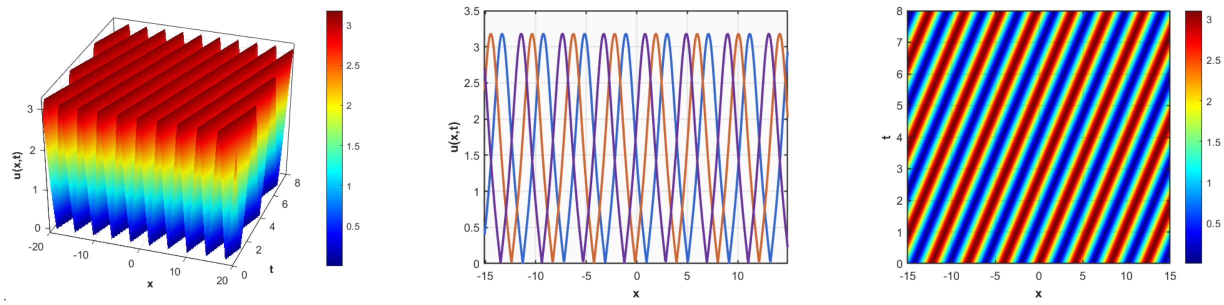

(a) 3D diagram. **(b)** 2D profiles. **(c)** Contour diagram.

Figure 1. Physical field profile $U(\xi)$ of the periodic traveling wave solution to Eq (2.1), reconstructed from $\Psi(\xi) = e_3 + (e_2 - e_3)\,\mathrm{sn}^2[\frac{1}{2}\sqrt{e_1 - e_3}(\xi - \xi_0); m_e]$ via $\Phi = \alpha^{-1}\Psi - \beta/(3\alpha)$ and $U = \sqrt{\Phi}$, with $\Delta > 0$ $(e_1 > e_2 > e_3)$. Parameters: $(\mu_1, \mu_2, \mu_3, k, l, m) = (1.0, 1.0, 0.5, 1.0, 0.5, 0.3)$, $A = 1.17$, $c = 1.5$, $E = 0.8$, $\chi_1 = -12.41$, $\chi_0 = 16.22$, $m_e = 0.901$. The reconstructed U is a periodic oscillatory profile (see the $\Delta > 0$ case in Section 3.3).

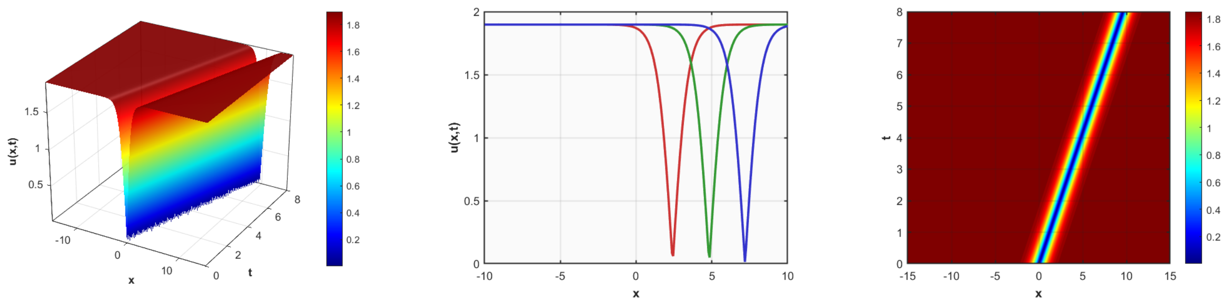

(a) 3D diagram. **(b)** 2D profiles. **(c)** Contour diagram.

Figure 2. Physical field profile $U(\xi)$ of the solitary traveling wave solution to Eq (2.1), reconstructed from $\Psi(\xi) = a - (a - b)\,\mathrm{sech}^2[\frac{1}{2}\sqrt{a - b}(\xi - \xi_0)]$ via $\Phi = \alpha^{-1}\Psi - \beta/(3\alpha)$ and $U = \sqrt{\Phi}$, with $\Delta = 0$ $(a > b)$. Parameters: $(\mu_1, \mu_2, \mu_3, k, l, m) = (1.0, 1.0, 0.5, 1.0, 0.5, 0.3)$, $A = 1.17$, $c = 1.2$, $E = -0.92$, $\chi_1 = -1.40$, $\chi_0 = -0.64$. The reconstructed U is a bell-shaped solitary pulse (see the $\Delta = 0$ double-root case in Section 3.3).

4. Global Hamiltonian geometry of the reduced system

Rewrite system Eq (2.4) as

$$\begin{cases} \dfrac{dU}{d\xi} = Y, \\ \dfrac{dY}{d\xi} = h_1\, U - h_2\, U^3, \end{cases} \tag{4.1}$$

where $h_1 = c/A$, $h_2 = \mu_1 k/(3A)$. Here, A is the effective dispersion along the traveling direction; h_1 measures the relative strength of wave speed to dispersion, and h_2 measures that of nonlinearity to dispersion. If μ_1, μ_2, μ_3, k, and c are all positive, then $A > 0$, and the system sits in the standard regime $h_1 > 0, h_2 > 0$. The remaining three sign combinations are mathematically admissible but require reversed propagation or nonlinearity signs. The associated Hamiltonian is

$$H(U,Y) = \frac{1}{2}Y^2 - \frac{h_1}{2}U^2 + \frac{h_2}{4}U^4 = E, \tag{4.2}$$

with E the energy constant.

4.1. Equilibria and their types

The equilibrium points satisfy $Y = 0$ and $h_1 U - h_2 U^3 = 0$. Thus,

$$P_0 = (0,0), \quad P_\pm = \left(\pm\sqrt{h_1/h_2}, 0\right), \tag{4.3}$$

with $P_\pm$ existing only when $h_1/h_2 > 0$ (i.e., h_1 and h_2 have the same sign).

The Jacobian matrix is

$$J(U,Y) = \begin{pmatrix} 0 & 1 \\ h_1 - 3h_2U^2 & 0 \end{pmatrix}.$$

The eigenvalues satisfy $\lambda^2 = h_1 - 3h_2U^2$, so the equilibrium types are determined by the signs of h_1 and h_2:

(1) If $h_1 > 0,\ h_2 > 0$, then P_0 is a saddle while $P_\pm$ are centers.
(2) If $h_1 < 0,\ h_2 < 0$, then P_0 is a center while $P_\pm$ are saddles.
(3) If $h_1 < 0,\ h_2 > 0$, then P_0 is the unique equilibrium and is a center.
(4) If $h_1 > 0,\ h_2 < 0$, then P_0 is the unique equilibrium and is a saddle.

The line $h_1 = 0$ is a pitchfork (symmetry-breaking) bifurcation boundary at which the linear part degenerates, and the finite phase portrait changes its topological structure.

4.2. Complete four-quadrant phase portrait classification

Based on the signs of h_1 and h_2, the reduced system exhibits four topologically distinct phase portraits, as detailed below. Figure 3 shows representative level sets of Eq (4.2) for the four regimes, computed with $|h_1| = |h_2| = 1$.

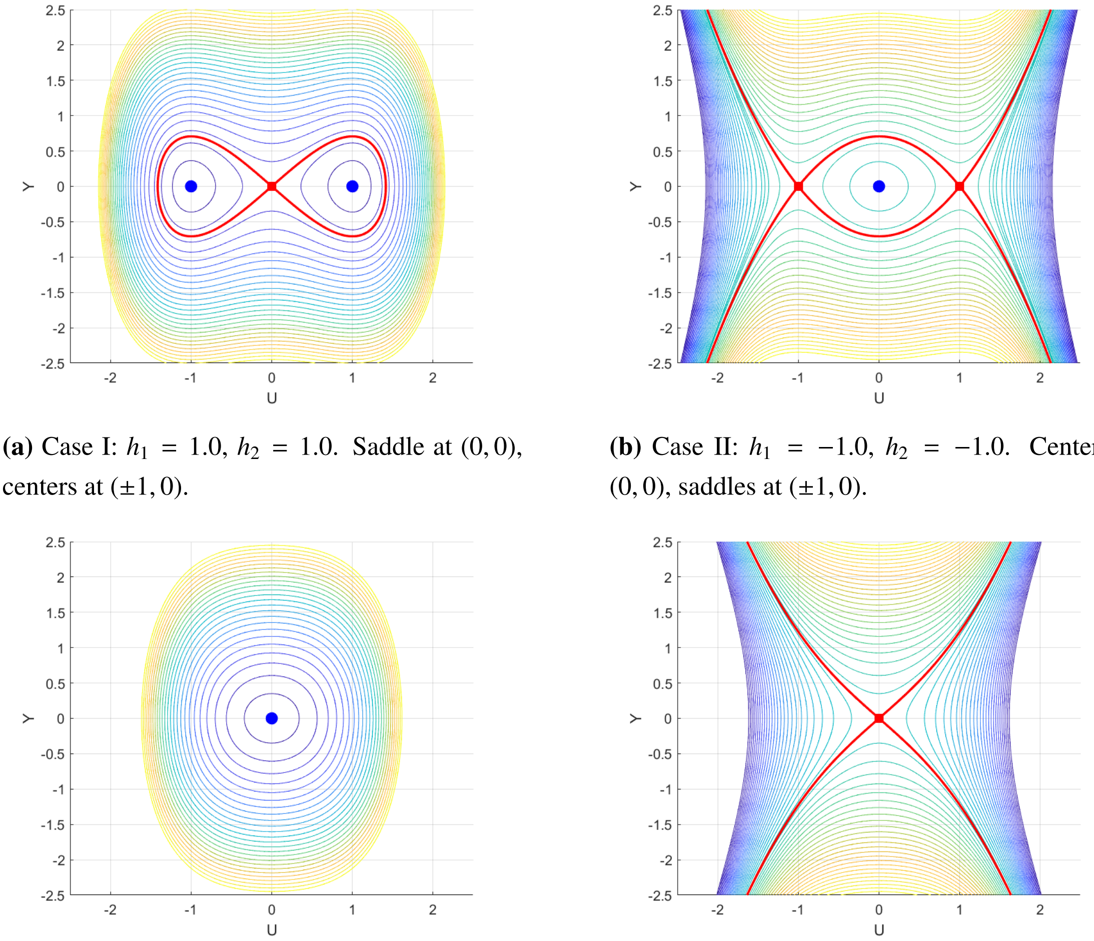

(a) Case I: $h_1 = 1.0$, $h_2 = 1.0$. Saddle at $(0, 0)$, centers at $(\pm 1, 0)$.

(b) Case II: $h_1 = -1.0$, $h_2 = -1.0$. Center at $(0, 0)$, saddles at $(\pm 1, 0)$.

(c) Case III: $h_1 = -1.0$, $h_2 = 1.0$. Global center at $(0, 0)$ with concentric periodic orbits.

(d) Case IV: $h_1 = 1.0$, $h_2 = -1.0$. Saddle at $(0, 0)$ with unbounded trajectories.

Figure 3. Phase portraits of the unforced system Eq (4.1) for the four parameter regimes.

Case I: $h_1 > 0, \; h_2 > 0$

The effective potential

$$V(U) = -\frac{h_1}{2}U^2 + \frac{h_2}{4}U^4 \tag{4.4}$$

yields a double-well potential, where P_0 is a saddle, and $P_\pm$ are symmetric centers. Their energy levels are

$$H(P_\pm) = -\frac{h_1^2}{4h_2} < 0 \tag{4.5}$$

for

$$-\frac{h_1^2}{4h_2} < E < 0, \tag{4.6}$$

two disjoint periodic orbit families surround P_+ and P_-. At $E = 0$, the saddle P_0 forms a symmetric figure-eight homoclinic separatrix. For $E > 0$, one outer periodic family encloses all three equilibria.

This regime yields localized pulse-type solitary waves (on the homoclinic orbit) and periodic waves (inside each well or outside the figure-eight separatrix).

Case II: $h_1 < 0,\ h_2 < 0$

Here,

$$V(U) = \frac{|h_1|}{2}U^2 - \frac{|h_2|}{4}U^4, \tag{4.7}$$

has a central well at $U = 0$ and symmetric maxima at

$$U = \pm\sqrt{\frac{|h_1|}{|h_2|}}. \tag{4.8}$$

The origin P_0 is a center, and $P_\pm$ are saddles, with saddle energy

$$H(P_\pm) = -\frac{h_1^2}{4h_2} > 0 \tag{4.9}$$

for

$$0 < E < -\frac{h_1^2}{4h_2}, \tag{4.10}$$

periodic orbits surround P_0. At

$$E = -\frac{h_1^2}{4h_2}, \tag{4.11}$$

heteroclinic connections link P_- and P_+. Energy levels with $E < 0$ or $E > -h_1^2/(4h_2)$ are unbounded.

This regime supports periodic waves near the center and kink/anti-kink waves on the heteroclinic threshold.

Case III: $h_1 < 0,\ h_2 > 0$

Here,

$$V(U) = \frac{|h_1|}{2}U^2 + \frac{h_2}{4}U^4. \tag{4.12}$$

The potential is positive definite and confining. The origin is the unique equilibrium and is a center. For every $E > 0$, the level set is a closed curve encircling the origin. Thus all finite, non-equilibrium trajectories are periodic, and P_0 acts as a global center in the finite plane.

Case IV: $h_1 > 0,\ h_2 < 0$

Now,

$$V(U) = -\frac{h_1}{2}U^2 - \frac{|h_2|}{4}U^4. \tag{4.13}$$

The potential decreases away from the origin and is unbounded below. The origin is the only equilibrium and is a saddle. No nontrivial bounded energy levels exist; all nonequilibrium trajectories are unbounded. Consequently, no bounded traveling waves arise from closed orbits or separatrix loops.

The signs of h_1 and h_2 determine the shape of the effective potential and therefore the global orbit geometry. All four cases are kept because together they exhaust the sign classification, but they are not equally realistic. Case I corresponds to positive wave speed, positive effective dispersion, and focusing cubic nonlinearity; the other three each require at least one sign reversal. Thus, unless a specific plasma parameterization is supplied, Cases II–IV should be viewed primarily as mathematically admissible regimes that complete the bifurcation picture.

4.3. Explicit homoclinic and heteroclinic orbits

The separatrix solutions can be obtained in closed form from the Hamiltonian level sets.
Homoclinic orbits (Case I). At the homoclinic energy level $E = 0$, integration gives

$$U_h^{\pm}(\xi) = \pm\sqrt{\frac{2h_1}{h_2}}\,\mathrm{sech}\left(\sqrt{h_1}(\xi-\xi_0)\right), \tag{4.14}$$

which correspond to bell-shaped solitary waves.
Heteroclinic orbits (Case II). At the heteroclinic energy level $E = -h_1^2/(4h_2)$, integration yields

$$U_k^{\pm}(\xi) = \pm\sqrt{\frac{h_1}{h_2}}\tanh\left(\sqrt{\frac{-h_1}{2}}(\xi-\xi_0)\right), \tag{4.15}$$

which correspond to kink and anti-kink traveling waves.

4.4. Dynamical interpretation of the wave families

The orbit classification yields the following wave correspondence: Closed orbits correspond to periodic traveling waves, the homoclinic loop in Case I corresponds to bell-shaped solitary waves, the heteroclinic connections in Case II correspond to kink and anti-kink waves as given explicitly by the tanh-type solutions in Eq (4.15), Case III yields only periodic bounded waves, and Case IV does not generate bounded traveling wave structures. The $\tan^2$-type branch in Case II(c) of Section 3.3 is not a heteroclinic wave but rather an unbounded singular periodic solution. This geometric interpretation complements the exact solution formulas in Section 3 and explains waveform selection through energy levels of the reduced phase plane.

5. Melnikov analysis for the periodically forced system

The periodic term is introduced as a weak phenomenological modulation compatible with the co-moving reduction. At the PDE level, a source depending on the traveling coordinate produces a harmonic term in the profile equation after one integration. It may represent the projection of a weak radio-frequency (RF) field or a periodic modulation of background density, magnetic field, or refractive index. The model is not claimed to be a unique first-principles forcing law; its role is to test the structural stability of the wave-organizing separatrices. To leading order, such influences enter the profile equation as a single small periodic term, yielding

$$u_t + \mu_1 u^2 u_x + \mu_2 u_{xxx} + \mu_3(u_{yy} + u_{zz})_x = \varepsilon R(\xi), \qquad 0 < \varepsilon \ll 1, \tag{5.1}$$

where R is the projection of the external driving onto the co-moving wave coordinate $\xi = kx+ly+mz-ct$. Substituting $u = U(\xi)$ and integrating once, as in Section 2, reduces this to

$$AU'' - cU + \frac{\mu_1 k}{3}U^3 = \varepsilon G(\xi) \tag{5.2}$$

with $G(\xi) = \int R(\xi)\,d\xi$.

For a harmonic modulation $G(\xi) = F\cos(\omega\xi)$, dividing Eq (5.2) by A and absorbing F/A into the amplitude gives the forced planar system

$$\begin{cases} \dfrac{dU}{d\xi} = Y, \\ \dfrac{dY}{d\xi} = h_1\, U - h_2\, U^3 + \varepsilon\cos(\omega\xi), \end{cases} \qquad 0 < \varepsilon \ll 1, \tag{5.3}$$

where ε now denotes the rescaled forcing amplitude $\varepsilon F/A$.

Here, ε measures the strength of the modulation and ω its frequency. Whatever physical reading is attached to them, Eq (5.3) answers one question: Do the homoclinic and heteroclinic connections survive a small time-periodic perturbation?

System Eq (5.3) is a time-periodic perturbation of Eq (4.1). The unperturbed flow possesses a homoclinic separatrix when $h_1 > 0, h_2 > 0$ and a heteroclinic separatrix when $h_1 < 0, h_2 < 0$. Melnikov theory is therefore applicable to detect transverse intersections of the stable and unstable manifolds, which indicate the onset of chaos.

5.1. Melnikov function

Writing Eq (5.3) in the standard perturbative form

$$\begin{cases} X' = f_0(X) + \varepsilon\, f_1(X, \xi), \\ X = (U, Y)^T, \end{cases} \tag{5.4}$$

with

$$\begin{cases} f_0(U, Y) = \begin{pmatrix} Y \\ h_1\, U - h_2\, U^3 \end{pmatrix}, \\ f_1(U, Y, \xi) = \begin{pmatrix} 0 \\ \cos(\omega\xi) \end{pmatrix}, \end{cases} \tag{5.5}$$

the Melnikov function associated with an unperturbed separatrix $X_s(\tau) = (U_s(\tau), Y_s(\tau))$ is defined by

$$M(\xi_0) = \int_{-\infty}^{\infty} Y_s(\tau)\cos(\omega(\tau + \xi_0))\, d\tau. \tag{5.6}$$

The signed distance between the perturbed stable and unstable manifolds on a transverse section is proportional to $\varepsilon M(\xi_0) + O(\varepsilon^2)$. A simple zero of M therefore implies a transverse intersection only for ε small enough; the expansion says nothing about orbit geometry or Lyapunov exponents at larger forcing.

5.2. Homoclinic case

By substituting the homoclinic orbit Eq (4.14) into Eq (5.6), it is first noted that

$$Y_h^{\pm}(\tau) = \mp\sqrt{\frac{2h_1^2}{h_2}}\,\operatorname{sech}(\sqrt{h_1}\,\tau)\tanh(\sqrt{h_1}\,\tau), \tag{5.7}$$

which is an odd function of τ. Using

$$\cos(\omega(\tau + \xi_0)) = \cos(\omega\tau)\cos(\omega\xi_0) - \sin(\omega\tau)\sin(\omega\xi_0), \tag{5.8}$$

the even cosine contribution vanishes after integration, and the following expression is obtained:

$$\begin{cases} M_h^{\pm}(\xi_0) = \pm C_h \sin(\omega\xi_0), \\ C_h = \pi\omega\sqrt{\dfrac{2}{h_2}}\,\mathrm{sech}(\dfrac{\pi\omega}{2\sqrt{h_1}}) > 0. \end{cases} \tag{5.9}$$

Hence, the zeros of the Melnikov function are

$$M_h^{\pm}(\xi_0) = 0 \iff \xi_0 = \frac{n\pi}{\omega}, \quad n \in \mathbb{Z}. \tag{5.10}$$

Moreover,

$$\frac{dM_h^{\pm}}{d\xi_0} = \pm C_h\omega\cos(\omega\xi_0), \tag{5.11}$$

which is nonzero at every zero of $M_h^{\pm}$. Therefore, all zeros are simple, and the perturbed stable and unstable manifolds intersect transversely for sufficiently small $0 < \varepsilon \ll 1$.

The factor $\mathrm{sech}(\pi\omega/(2\sqrt{h_1}))$ shows that the splitting amplitude decays exponentially as ω increases relative to the inverse width of the homoclinic pulse. The splitting is therefore weakest at high frequency. In the homoclinic case, the amplitude also vanishes as $\omega \to 0$, so C_h attains its maximum at an intermediate frequency rather than at low frequency; the heteroclinic case behaves differently and is discussed in Section 5.5.

5.3. Heteroclinic case

Substituting the heteroclinic orbit Eq (4.15) into Eq (5.6) gives

$$Y_k^{\pm}(\tau) = \pm\sqrt{\frac{-h_1^2}{2h_2}}\,\mathrm{sech}^2\left(\sqrt{\frac{-h_1}{2}}\tau\right), \tag{5.12}$$

which is an even function of τ. Therefore, the odd sine contribution vanishes, and the Melnikov function becomes

$$\begin{cases} M_k^{\pm}(\xi_0) = \pm C_k \cos(\omega\xi_0), \\ C_k = \pi\omega\sqrt{\dfrac{2}{-h_2}}\,\mathrm{csch}(\dfrac{\pi\omega}{\sqrt{-2h_1}}) > 0. \end{cases} \tag{5.13}$$

Its zeros satisfy

$$M_k^{\pm}(\xi_0) = 0 \iff \xi_0 = \frac{\pi/2 + n\pi}{\omega}, \quad n \in \mathbb{Z}. \tag{5.14}$$

Furthermore,

$$\frac{dM_k^{\pm}}{d\xi_0} = \mp C_k\omega\sin(\omega\xi_0), \tag{5.15}$$

which is nonzero at every zero of $M_k^{\pm}$. Hence, all zeros are simple, and the stable and unstable manifolds intersect transversely in the perturbed heteroclinic regime.

5.4. Consequence for chaotic dynamics

Therefore, for sufficiently small $0 < \varepsilon \ll 1$, the homoclinic loop in Case I and the heteroclinic cycle in Case II split transversely whenever the corresponding Melnikov function has a simple zero. In the homoclinic case, the Smale-Birkhoff homoclinic theorem implies the existence of a Smale horseshoe and hence chaotic dynamics. In the heteroclinic case, the transverse splitting of the heteroclinic cycle likewise generates a heteroclinic tangle and chaotic dynamics. The remaining parameter regimes (Cases III and IV) do not admit separatrix-based Melnikov analysis, because the unperturbed system has no homoclinic or heteroclinic orbit.

5.5. Melnikov amplitude decay

The Melnikov amplitudes are given explicitly by

$$\begin{cases} C_h(\omega) = \pi\omega\sqrt{\dfrac{2}{h_2}}\,\mathrm{sech}(\dfrac{\pi\omega}{2\sqrt{h_1}}), & h_1, h_2 > 0, \\ C_k(\omega) = \pi\omega\sqrt{\dfrac{2}{-h_2}}\,\mathrm{csch}(\dfrac{\pi\omega}{\sqrt{-2h_1}}), & h_1, h_2 < 0. \end{cases} \tag{5.16}$$

The asymptotic behavior differs between the two branches. For the homoclinic case, $C_h(\omega) \to 0$ as $\omega \to 0$, attains a maximum at an intermediate frequency, and decays exponentially as $\omega \to \infty$. For the heteroclinic case, $C_k(\omega) \to 2\sqrt{h_1/h_2}$ as $\omega \to 0$ (with $h_1, h_2 < 0$, so the ratio is positive) and decays exponentially as $\omega \to \infty$. The two branches therefore behave oppositely at low frequency: C_k approaches a finite positive limit, whereas C_h vanishes. In the low-frequency limit it is therefore the heteroclinic separatrix, not the homoclinic one, that splits more readily. Figure 4 plots the two amplitudes in Eq (5.16) against the forcing frequency on linear and logarithmic scales, with $|h_1| = |h_2| = 1$. The contrast at low frequency and the common exponential decay at high frequency are both visible.

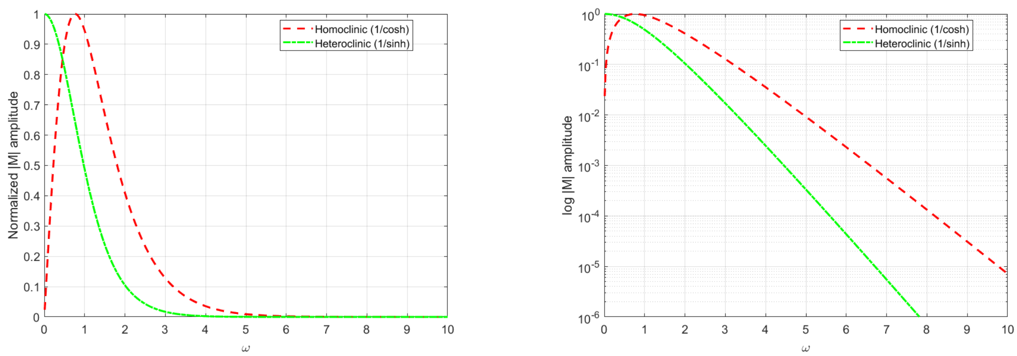

(a) Linear scale. **(b)** Log scale.

Figure 4. Melnikov amplitude decay as a function of the forcing frequency ω. The red curve corresponds to the homoclinic case, $C_h(\omega) = \pi\omega\sqrt{2/h_2}\,\mathrm{sech}(\pi\omega/(2\sqrt{h_1}))$. The green curve corresponds to the heteroclinic case, $C_k(\omega) = \pi\omega\sqrt{2/(-h_2)}\,\mathrm{csch}(\pi\omega/\sqrt{-2h_1})$. The horizontal axis is the forcing frequency; the vertical axis is the normalized amplitude. Amplitudes are normalized by their respective maxima; normalization does not affect exponential decay in the log-scale panel.

These formulas show that the first-order separatrix-splitting amplitude decays as ω increases. They should therefore be interpreted as a small-forcing criterion for the ease of separatrix splitting, rather than as a standalone predictor of the responses reported in Section 6. There the frequency is held fixed at $\omega = \sqrt{2}$, and only the amplitude is varied, which is the comparison the first-order theory supports.

6. Chaotic behavior and sensitivity analysis

Section 5 predicts transverse splitting for small ε but says nothing about what an individual orbit then looks like. This section supplies that information. Stroboscopic Poincaré sections and largest Lyapunov exponents are computed for $\varepsilon = 0.01, 0.05$, and 0.10 at fixed $\omega = \sqrt{2}$, using the same integrator, step size, and averaging window throughout, and the response to nearby initial states is examined at $\varepsilon = 0.10$. The numerical picture is consistent with the Melnikov prediction, with one qualification: At the smallest amplitude, the selected orbit remains regular, as a transverse tangle need not be visible along every trajectory.

6.1. Phase-plane trajectories and stroboscopic Poincaré sections

Figure 5 shows the phase-plane trajectories at the three amplitudes, with the initial condition fixed at $(U_0, Y_0) = (0.2, 0.1)$. As ε grows, the orbit spreads outward and begins to cross between the two wells.

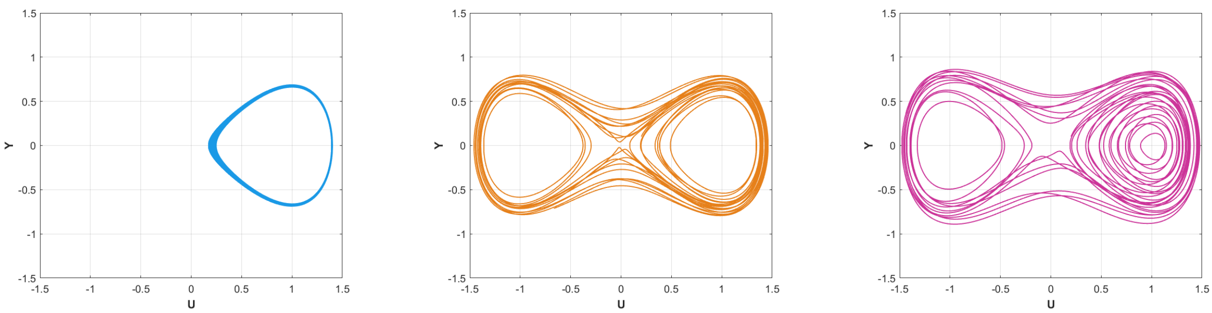

(a) $\varepsilon = 0.01$. **(b)** $\varepsilon = 0.05$. **(c)** $\varepsilon = 0.10$.

Figure 5. Phase-plane trajectories of the periodically forced system Eq (5.3) with $h_1 = h_2 = 1$, $\omega = \sqrt{2}$, and initial condition $(U_0, Y_0) = (0.2, 0.1)$.

For a system of period $T = 2\pi/\omega$, the stroboscopic section is the discrete set

$$\mathcal{P} = \left\{ (U(\xi_n),\ Y(\xi_n)) \in \mathbb{R}^2 \mid \xi_n = \frac{2n\pi}{\omega},\ n \in \mathbb{N} \right\}, \tag{6.1}$$

with ξ_n denoting the sampling times, one per forcing period. The structure of $\mathcal{P}$ separates the three regimes: A periodic orbit leaves finitely many isolated points, quasiperiodic motion leaves a smooth closed curve, and motion inside a separatrix layer leaves a scattered two-dimensional band.

The same three trajectories are sampled once per forcing period at $\xi = 2n\pi/\omega$, with the first 100 periods discarded and 2500 points retained. All three panels share identical coordinate ranges $U \in [-1.65, 1.65]$ and $Y \in [-1.05, 1.05]$, ensuring that the spread of the point sets is not masked by automatic scaling. The results are presented in Figure 6.

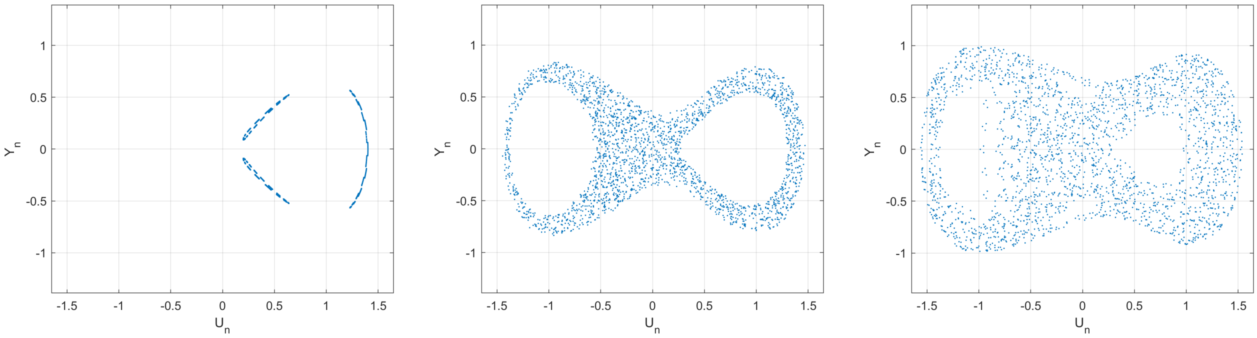

(a) $\varepsilon = 0.01$. **(b)** $\varepsilon = 0.05$. **(c)** $\varepsilon = 0.10$.

Figure 6. Stroboscopic Poincaré sections of the periodically forced system Eq (5.3) with $h_1 = h_2 = 1$, $\omega = \sqrt{2}$ and initial condition $(U_0, Y_0) = (0.2, 0.1)$. After discarding 100 transient forcing periods, 2500 points are sampled once per period using a fixed-step RK4 integrator with 800 steps per period. All three panels share identical coordinate ranges.

As ε increases, the Poincaré sections in Figure 6 exhibit a transition from regular structures to chaotic layers. For $\varepsilon = 0.01$, the section is confined to thin, smooth arcs; the point set does not fill a two-dimensional region but instead concentrates on several well-separated smooth invariant curves, indicating that the orbit is in a regular or near-resonant state. For $\varepsilon = 0.05$, the section undergoes a qualitative transition: the point set transforms from one-dimensional thin curves into a two-dimensional scattered band surrounding the former figure-eight separatrix, with trajectories visiting both potential wells. At finite resolution this is consistent with a chaotic layer generated by separatrix splitting. For $\varepsilon = 0.10$, the scattered region expands further into a wider stochastic sea, with the points occupying a larger area and exhibiting high occupancy in both potential wells and the central crossing region.

6.2. *Largest Lyapunov exponent*

The largest Lyapunov exponent (LLE) is computed using the Benettin algorithm [45] to quantify the sensitivity of the forced system to initial conditions. The variational equations associated with the forced system Eq (5.3) are

$$\delta U' = \delta Y, \qquad \delta Y' = \left(h_1 - 3h_2 U^2\right)\delta U, \tag{6.2}$$

which govern the linearized evolution of an infinitesimal perturbation $(\delta U, \delta Y)$ along a reference trajectory (U, Y). The LLE is defined as

$$\lambda_{\max} = \lim_{\xi\to\infty} \frac{1}{\xi} \ln \frac{\|\boldsymbol{\delta}(\xi)\|}{\|\boldsymbol{\delta}(0)\|}, \tag{6.3}$$

where $\boldsymbol{\delta} = (\delta U, \delta Y)^T$. The integration is carried out using the same fixed-step RK4 integrator as for the Poincaré sections, with 800 steps per forcing period and renormalization applied four times per period. The first 100 forcing periods are discarded as transient, and the LLE is averaged over 2500 periods. The initial tangent vector is chosen as $\boldsymbol{\delta}(0) = (1, 0)^T$. Convergence checks with halved step size and doubled integration time confirm that the reported $\lambda_{\max}$ values are stable at the qualitative level; the variations are smaller than the differences between the three forcing amplitudes. Table 1 collects the largest Lyapunov exponent together with the coordinate ranges of the stroboscopic point set for the three forcing amplitudes. The exponent rises by three orders of magnitude between $\varepsilon = 0.01$ and $\varepsilon = 0.05$, and over the same step the point set expands from a single well ($U_{\min} = 0.1986$) to both wells ($U_{\min} = -1.4518$), which is the transition already visible in Figure 6.

Table 1. Summary of numerical results for the stroboscopic Poincaré sections and largest Lyapunov exponents, all computed under consistent numerical settings.

ε	$\lambda_{\max}$	$U_{\min}$	$U_{\max}$	$Y_{\min}$	$Y_{\max}$
0.01	2.73×10^{-4}	0.1986	1.4024	−0.5666	0.5666
0.05	1.126×10^{-1}	−1.4518	1.4677	−0.8638	0.8638
0.10	1.199×10^{-1}	−1.5689	1.5231	−0.9791	0.9747

The convergence of the finite-time LLE as a function of the averaging window is shown in Figure 7 for the same three trajectories. For $\varepsilon = 0.05$ and 0.10, the finite-time exponent stays positive over the whole averaging window and settles near 0.11 and 0.12. For $\varepsilon = 0.01$, it decays to order 10^{-4}, which at this resolution cannot be distinguished from zero.

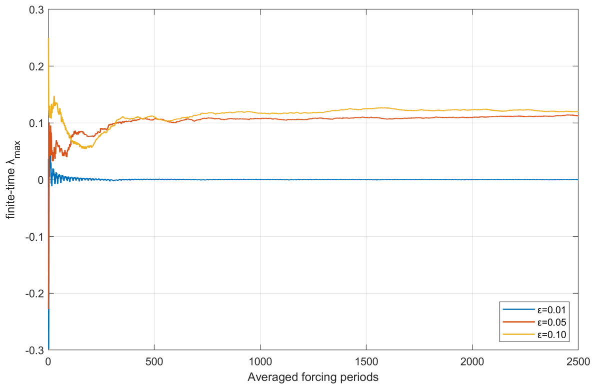

Figure 7. Convergence of the finite-time largest Lyapunov exponent as a function of the averaging window for the three forcing amplitudes. The curves are computed under identical numerical settings as the Poincaré sections in Figure 6. For $\varepsilon = 0.05$ and 0.10, the exponents converge to positive values, while for $\varepsilon = 0.01$, the exponent decays to the order of 10^{-4}, numerically indistinguishable from zero.

The two diagnostics answer different questions. A section shows how the orbit is organized under the period map; the exponent says whether nearby orbits separate exponentially along it. Neither alone is decisive, as a thin arc and a scattered band can both occur at finite resolution, but the positive exponents at $\varepsilon = 0.05$ and 0.10 and the scattered sections in Figure 6 point the same way.

6.3. Sensitivity to initial conditions

The positive exponent at $\varepsilon = 0.10$ should show up as visible divergence between neighboring orbits. Figure 8 tests this at the same ε and ω for three nearby initial states: $(U_0, Y_0) = (0.20, 0.10)$, $(0.21, 0.10)$, and $(0.20, 0.11)$.

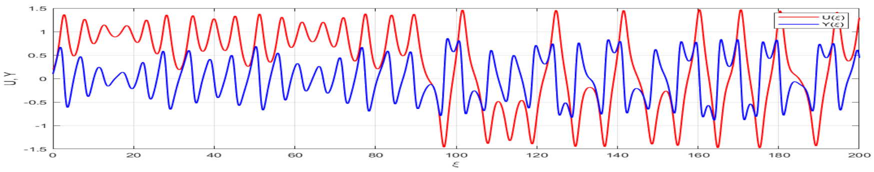

(a) $(U_0, Y_0) = (0.20, 0.10)$.

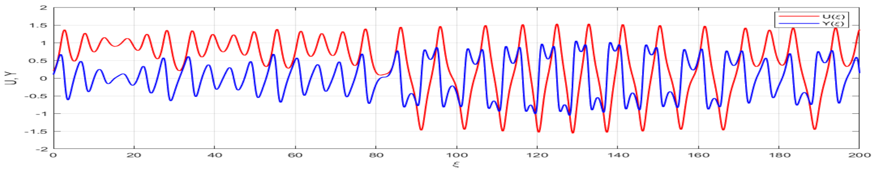

(b) $(U_0, Y_0) = (0.21, 0.10)$.

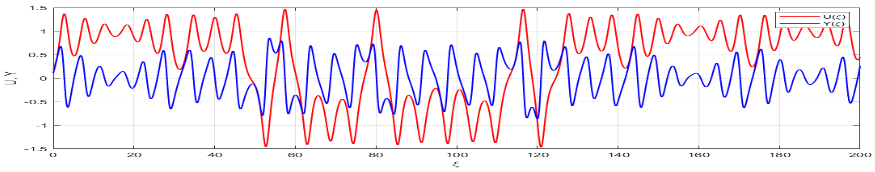

(c) $(U_0, Y_0) = (0.20, 0.11)$.

Figure 8. Sensitivity to initial conditions in the small-forcing regime ($\varepsilon = 0.10$, $\omega = \sqrt{2}$). Three nearby initial states (a)–(c) separate visibly within the window $\xi \in [0, 200]$.

As shown in Figure 8, the resulting trajectories diverge over the observation window $\xi \in [0, 200]$, despite the small differences in the initial states. The largest deviation occurs for trajectory (c), whose perturbation acts in the Y-direction. The Euclidean separation $\|(\Delta U, \Delta Y)\|$ between each perturbed orbit and the reference orbit reaches $O(1)$ over $\xi \in [0, 200]$, consistent with the positive exponent $\lambda_{\max}$ reported in Section 6.2. Over a finite window, such divergence is suggestive rather than conclusive, and it is the positive exponent of Section 6.2 that makes the reading firm.

7. Conclusions

The traveling-wave reduction organizes mKdV-ZK dynamics through a quartic effective potential. Its four sign regimes separate periodic families, figure-eight homoclinic pulses, heteroclinic kink connections, and parameter ranges carrying no bounded wave at all. The amplitude-squared substitution gives a convenient cubic description of a restricted set of explicit profiles, provided the constraint $\Phi \geq 0$ and the sign reconstruction of U are respected. This part of the analysis recovers the traveling-wave geometry already known for this model.

The contribution of this article lies in the forced problem. For a weak periodic modulation the Melnikov functions on the homoclinic and on the heteroclinic separatrix can both be written in closed form. Their simple zeros give transverse splitting criteria, and their amplitudes differ in the low-frequency limit while sharing an exponential decay at high frequency. Stroboscopic Poincaré sections and largest Lyapunov exponents computed at $\varepsilon = 0.01$, 0.05, and 0.10 are consistent with this mechanism: The section breaks up into a scattered layer around the former separatrix at the same amplitudes for which the exponent becomes positive.

Two restrictions should be kept in mind. The analysis is confined to the symmetric branch $C_0 = 0$, and the periodic source is phenomenological rather than derived from a complete plasma model; the Melnikov criterion itself is a first-order result and carries no information about strong forcing. Nonzero integration constants, damping, variable coefficients, stochastic excitation, and fractional or nonlocal extensions each lead to a different problem and are natural directions for further work.

Author contributions

Junjie Li: Conceptualization, resources, writing—review and editing, supervision, project administration and funding acquisition; Jiaye Lin: Conceptualization, methodology, validation, formal analysis, data curation, writing—original draft preparation, writing—review and editing and visualization; Yucheng Chen: Conceptualization, resources, writing—review and editing, supervision, project administration and funding acquisition; Yaling Lai: Software, validation and investigation; Xiyan Wu: Validation; Changlong Chen: Writing—review and editing, supervision and project administration. All authors have read and agreed to the published version of the manuscript.

Use of Generative-AI tools declaration

The authors declare they have not used Artificial Intelligence (AI) tools in the creation of this article.

Acknowledgments

This work was supported by the Natural Science Foundation of Fujian Province (Grant No. 2023J011434) and the Industry-University-Research Cooperation Project of Xiamen City (Grant No. 2023CXYO424).

Conflict of interest

The authors declare there are no conflicts of interest.

References

1. S. Duran, An investigation of the physical dynamics of a traveling-wave solution called a bright soliton, *Phys. Scr.*, **96** (2021), 125251. https://doi.org/10.1088/1402-4896/ac37a1
2. S. Duran, A. Yokus, G. Kilinc, A study on solitary wave solutions for the Zoomeron equation supported by two-dimensional dynamics, *Phys. Scr.*, **98** (2023), 125265. https://doi.org/10.1088/1402-4896/ad0c3c
3. A. R. Seadawy, A. Ali, M. A. Helal, Analytical wave solutions of the (2+1)-dimensional Boiti-Leon-Pempinelli and Boiti-Leon-Manna-Pempinelli equations by mathematical methods, *Math. Methods Appl. Sci.*, **44** (2021), 14292–14315. https://doi.org/10.1002/mma.7697
4. J. G. Liu, Q. Ye, Stripe solitons and lump solutions for a generalized Kadomtsev-Petviashvili equation with variable coefficients in fluid mechanics, *Nonlinear Dyn.*, **96** (2019), 23–29. https://doi.org/10.1007/s11071-019-04770-8

5. A. M. Wazwaz, *Partial differential equations and solitary waves theory*, Berlin: Springer, 2009. https://doi.org/10.1007/978-3-642-00251-9
6. G. Chen, J. L. Moiola, An overview of bifurcation, chaos and nonlinear dynamics in control systems, *J. Franklin Inst.*, **331** (1994), 819–858. https://doi.org/10.1016/0016-0032(94)90090-6
7. X. Zhao, H. Zhou, Y. Tang, H. Jia, Travelling wave solutions for modified Zakharov-Kuznetsov equation, *Appl. Math. Comput.*, **181** (2006), 634–648. https://doi.org/10.1016/j.amc.2006.01.049
8. B. B. Kadomtsev, V. I. Petviashvili, On the stability of solitary waves in weakly dispersing media, *Sov. Phys. Dokl.*, **15** (1970), 539–541.
9. V. E. Zakharov, E. A. Kuznetsov, On three dimensional solitons, *Sov. Phys. JETP*, **39** (1974), 285–288.
10. D. J. Korteweg, G. de Vries, On the change of form of long waves advancing in a rectangular canal, and on a new type of long stationary waves, *Philos. Mag.*, **91** (2011), 1007–1028. https://doi.org/10.1080/14786435.2010.547337
11. A. R. Seadawy, Three-dimensional nonlinear modified Zakharov-Kuznetsov equation of ion-acoustic waves in a magnetized plasma, *Comput. Math. Appl.*, **71** (2016), 201–212. https://doi.org/10.1016/j.camwa.2015.11.006
12. M. R. Pervin, H. O. Roshid, P. Dey, S. S. Shanta, S. Kumar, Ion acoustic solitary wave solutions to mKdV-ZK model in homogeneous magnetized plasma, *Adv. Math. Phys.*, **2023** (2023), 1901898. https://doi.org/10.1155/2023/1901898
13. A. J. Pan-Collantes, C. Muriel, A. Ruiz, Classification of traveling wave solutions of the modified Zakharov-Kuznetsov equation, *Chaos Solitons Fract.*, **193** (2025), 116091. https://doi.org/10.1016/j.chaos.2025.116091
14. H. R. Nabi, H. F. Ismael, N. A. Shah, W. Weera, W-shaped soliton solutions to the modified Zakharov-Kuznetsov equation of ion-acoustic waves in (3+1)-dimensions arise in a magnetized plasma, *AIMS Math.*, **8** (2023), 4467–4486. https://doi.org/10.3934/math.2023222
15. G. Wu, Y. Guo, Y. Yu, New processing technique of Jacobian elliptic equation and its application to the (3+1)-dimensional modified Korteweg-de Vries-Zakharov-Kuznetsov equation, *Symmetry*, **16** (2024), 1285. https://doi.org/10.3390/sym16101285
16. A. E. Hamza, O. Osman, M. U. Sarwar, K. Aldwoah, H. Saber, M. Hleili, Exploring solitons solutions of a (3+1)-dimensional fractional mKdV-ZK equation, *Fractal Fract.*, **8** (2024), 498. https://doi.org/10.3390/fractalfract8090498
17. S. M. Y. Arafat, M. Asif, M. M. Rahman, Nonlinear dynamic wave properties of travelling wave solutions in (3+1)-dimensional mKdV-ZK model, *PLoS ONE*, **20** (2025), e0306734. https://doi.org/10.1371/journal.pone.0306734
18. S. Zhao, J. Feng, Chaotic dynamics and some solutions for the (n+1)-dimensional modified Zakharov-Kuznetsov equation in plasma physics, *Open Phys.*, **23** (2025), 20250159. https://doi.org/10.1515/phys-2025-0159
19. K. Nonlaopon, N. Mann, S. Kumar, S. Rezaei, M. A. Abdou, A variety of closed-form solutions, Painlevé analysis, and solitary wave profiles for modified KdV-Zakharov-Kuznetsov equation in (3+1)-dimensions, *Results Phys.*, **36** (2022), 105394. https://doi.org/10.1016/j.rinp.2022.105394

20. S. Malik, S. Kumar, A. Das, A (2+1)-dimensional combined KdV-mKdV equation: integrability, stability analysis and soliton solutions, *Nonlinear Dyn.*, **107** (2022), 2689–2701. https://doi.org/10.1007/s11071-021-07075-x
21. M. A. Abdou, A generalized auxiliary equation method and its applications, *Nonlinear Dyn.*, **52** (2008), 95–102. https://doi.org/10.1007/s11071-007-9261-y
22. M. Ozisik, A. Secer, M. Bayram, The bell-shaped perturbed dispersive optical solitons of Biswas-Arshed equation using the new Kudryashov's approach, *Optik*, **267** (2022), 169650. https://doi.org/10.1016/j.ijleo.2022.169650
23. S. Duran, H. Durur, A. Yokus, Traveling wave and general form solutions for the coupled Higgs system, *Math. Methods Appl. Sci.*, **46** (2023), 8915–8933. https://doi.org/10.1002/mma.9024
24. A. Yokus, S. Duran, D. Kaya, An expansion method for generating travelling wave solutions for the (2+1)-dimensional Bogoyavlensky-Konopelchenko equation with variable coefficients, *Chaos Solitons Fract.*, **178** (2024), 114316. https://doi.org/10.1016/j.chaos.2023.114316
25. E. M. E. Zayed, M. E. M. Alngar, M. M. El-Horbaty, A. Biswas, A. H. Kara, Y. Yildirim, et al., Cubic-quartic polarized optical solitons and conservation laws for perturbed Fokas-Lenells model, *J. Nonlinear Opt. Phys. Mater.*, **30** (2021), 2150005. https://doi.org/10.1142/S0218863521500053
26. A. Saha, S. B. G. Karakoç, K. K. Ali, New exact soliton solutions and multistability for the modified Zakharov-Kuznetsov equation with higher order dispersion, *Math. Sci. Appl. E-Notes*, **11** (2023), 226–240. https://doi.org/10.36753/mathenot.1180832
27. K. Hosseini, F. Samadani, D. Kumar, M. Faridi, New optical solitons of cubic-quartic nonlinear Schrödinger equation, *Optik*, **157** (2018), 1101–1105. https://doi.org/10.1016/j.ijleo.2017.11.124
28. S. Zhao, Z. Li, Bifurcation, chaotic behavior, and traveling wave solutions of the space-time fractional Zakharov-Kuznetsov-Benjamin-Bona-Mahony equation, *Front. Phys.*, **13** (2025), 1502570. https://doi.org/10.3389/fphy.2025.1502570
29. K. Basheer, A. F. Hashem, M. Arshad, M. Nadeem, A. S. Al-Moisheer, A. R. Seadawy, Bifurcation, chaos, sensitivity analysis, and dynamics of the (3+1)-dimensional nonlinear extended Zakharov-Kuznetsov equation and its applications, *J. Nonlinear Math. Phys.*, **33** (2026), 6. https://doi.org/10.1007/s44198-025-00361-x
30. S. Yang, Bifurcation of travelling wave solutions for (3+1)-dimensional mKdV-ZK equation, *Sch. J. Phys. Math. Stat.*, **9** (2022), 109–121. https://doi.org/10.36347/sjpms.2022.v09i07.002
31. Y. Song, Y. Ma, B. Yang, Z. Wang, Exact solutions and bifurcations for the (3+1)-dimensional generalized KdV-ZK equation, *Phys. Scr.*, **99** (2024), 075205. https://doi.org/10.1088/1402-4896/ad4e14
32. F. S. Alshammari, H. O. Roshid, A. S. Alkhorayef, A. A. Elsadany, A. Aldurayhim, Dynamics of solitary waves, chaotic behaviors, and Jacobi elliptic wave solutions in telecommunication systems, *Results Phys.*, **60** (2024), 107629. https://doi.org/10.1016/j.rinp.2024.107629
33. J. L. Yin, Q. Q. Xing, L. X. Tian, Melnikov analysis and chaos control of nonlinear dispersive KdV equation under external periodic perturbation, *Indian J. Phys.*, **89** (2015), 273–279. https://doi.org/10.1007/s12648-014-0556-9

34. A. H. Arnous, Qualitative dynamics and homoclinic chaos in a stochastic Klein-Gordon-Schrödinger system, *Qual. Theory Dyn. Syst.*, **24** (2025), 235. https://doi.org/10.1007/s12346-025-01395-8

35. V. K. Melnikov, On the stability of the center for time periodic perturbations, *Trans. Moscow Math. Soc.*, **12** (1963), 1–57.

36. S. Wiggins, *Introduction to applied nonlinear dynamical systems and chaos*, New York: Springer, 2003. https://doi.org/10.1007/b97481

37. J. Guckenheimer, P. Holmes, *Nonlinear oscillations, dynamical systems, and bifurcations of vector fields*, New York: Springer, 2013. https://doi.org/10.1007/978-1-4612-1140-2

38. C. Chicone, Homoclinic orbits, Melnikov's method, and chaos, In *Ordinary differential equations with applications*, New York: Springer, 2024. https://doi.org/10.1007/978-3-031-51652-8

39. K. J. Wang, J. Si, Optical solitons to the Radhakrishnan-Kundu-Lakshmanan equation by two effective approaches, *Eur. Phys. J. Plus*, **137** (2022), 1016. https://doi.org/10.1140/epjp/s13360-022-03239-9

40. K. J. Wang, Abundant exact soliton solutions to the Fokas system, *Optik*, **249** (2022), 168265. https://doi.org/10.1016/j.ijleo.2021.168265

41. N. Alam, M. S. Ullah, T. A. Nofal, H. M. Ahmed, K. K. Ahmed, M. A. AL-Nahhas, Novel dynamics of the fractional KFG equation through the unified and unified solver schemes with stability and multistability analysis, *Nonlinear Eng.*, **13** (2024), 20240034. https://doi.org/10.1515/nleng-2024-0034

42. M. Madadi, L. Akinyemi, Determinant solitons and rational lump waves in a (3+1)-dimensional extended Korteweg-de Vries equation, *Wave Motion*, **147** (2026), 103782. https://doi.org/10.1016/j.wavemoti.2026.103782

43. K. J. Wang, G. D. Wang, Study on the nonlinear vibration of embedded carbon nanotube via the Hamiltonian-based method, *J. Low Freq. Noise Vib. Act. Control*, **41** (2022), 112–117. https://doi.org/10.1177/14613484211032757

44. K. J. Wang, Dynamic properties of large amplitude nonlinear oscillations using Hamiltonian-based frequency formulation, *Kuwait J. Sci.*, **51** (2024), 100186. https://doi.org/10.1016/j.kjs.2024.100186

45. G. Benettin, L. Galgani, A. Giorgilli, J. M. Strelcyn, Lyapunov characteristic exponents for smooth dynamical systems and for Hamiltonian systems; a method for computing all of them. Part 1: Theory, *Meccanica*, **15** (1980), 9–20. https://doi.org/10.1007/BF02128236